Electronic structure of the altermagnet candidate $FeSb_2$: High-field torque magnetometry and density functional theory studies

Cole Phillips,[1,*] Ganesh Pokharel,[2,*] Kyryl Shtefiienko,[1,*] Shalika R. Bhandari,[3] David E. Graf,[4,5] D. P. Rai,[6,†] and Keshav Shrestha[1,‡]

[1]*Department of Chemistry and Physics, West Texas A&M University, Canyon, Texas 79016, USA*
[2]*Perry College of Mathematics, Computing, and Sciences, University of West Georgia, Carrollton, Georgia 30118, USA*
[3]*Department of Physics, Bhairahawa Multiple Campus, Tribhuvan University, Bhairahawa 32900, Nepal*
[4]*Department of Physics, Florida State University, Tallahassee, Florida 32306, USA*
[5]*National High Magnetic Field Laboratory, Tallahassee, Florida 32310, USA*
[6]*Department of Physics, Mizoram University, Aizawl 796004, India*

(Received 13 November 2024; revised 3 January 2025; accepted 3 February 2025; published 18 February 2025)

This study explores the synthesis and electronic structure of $FeSb_2$, an altermagnet (AM) candidate, through torque magnetometry and *ab initio* density functional theory calculations. The temperature-dependent magnetic susceptibility data reveal an antiferromagnetic ground state below room temperature. To probe its electronic properties, we conducted high-field torque magnetometry up to 41 T and observed clear de Haas–van Alphen (dHvA) oscillation with a major peak at 65 T. Angular and temperature-dependent dHvA measurements were further conducted to map the Fermi surface parameters of $FeSb_2$. Interestingly, the spin-polarized electronic bands display asymmetric behavior between spin-up and spin-down states. The presence of a nonrelativistic spin splitting band in the collinear antiferromagnet depicted a strong evidence of altermagnetism in $FeSb_2$. Three bands intersect the Fermi level, forming the Fermi surface of $FeSb_2$. The band-resolved Fermi pockets exhibit d-wave symmetry and display asymmetry between the spin-up and spin-down states. These findings provide valuable insights into the electronic and magnetic structure of $FeSb_2$ and strongly support its classification as an AM.

DOI: 10.1103/PhysRevB.111.075141

I. INTRODUCTION

Recently, a unique magnetic phase having the combined properties of both ferromagnet (FM) and antiferromagnet (AFM) has been discovered and named altermagnet (AM) [1]. A prototype AM, RuO_2, exhibits broken time-reversal symmetry and a spontaneous Hall effect, similar to that of a conventional FM, despite having compensated collinear antiferromagnetic coupling between the Ru atoms, which feature motif-pair anisotropy (noninterconvertible spin-structure motif pair) [2–4]. In general, collinear AFMs are protected by time-reversal symmetry ($\mathcal{T}$) and inhibit the anomalous Nernst effect, as well as the anomalous thermal Hall effect [5]. In contrast, the breaking of $\mathcal{PT}$ ($\mathcal{P}$ refers to spatial inversion or translation), owing to their anisotropic local environment, results in the crystal Hall effect within an AM. Subsequently, Feng *et al.* experimentally confirmed this unusual magnetic ordering by calculating an anomalous Hall conductivity of $\sim$1000 $\Omega^{-1}\,\mathrm{cm}^{-1}$ in RuO_2 [6]. Other than the bulk, ground-state compensated magnetic behavior was also found in the thin film of rutile RuO_2 from the resonant x-ray scattering measurements [7]. So far, several AMs have been reported with hybrid characteristics of both ferromagnet (broken time-reversal symmetry, lack of the nonrelativistic degeneracy in the first Brillouin zone, presence of the anomalous Hall effect, spin torque, finite magneto-optical effect) and AFM (collinear antiferromagnetic coupling with net zero magnetization) [3,4,6,8–18].

The nonrelativistic spin-splitting (NRSS) band in collinear AM RuO_2 is rather intriguing. Although NRSS in AM is a distinctive feature, there are very few theories to explain the emergence of such phenomena in terms of electron behavior in the presence of an intrinsic magnetic field. Yuan *et al.* reported that spin density ($d/g/i$ wave) is responsible for such splitting, due to spin-broken symmetry and motif-pair anisotropy under certain symmetry conditions [4]. McClarty and Rau recently proposed that the origin of d-wave AM is related to the multipolar secondary order (octupole moment) in the Néel phase [13]. Bhowal and Spaldin describe the NRSS (d-wave spin splitting) in centrosymmetric antiferromagnets MnF_2 with the similar concept of the higher-order multipoles such as O_{32-} octupoles analogous to a conventional ferromagnetic dipole [19]. The NRSS band in momentum space complements the Zeeman effect and spin-orbit couplings (SOC). In particular, within AFMs, SOC plays a crucial role in mediating spin-momentum locking and facilitating various physical properties essential for spintronics [20]. FMs are preferred materials for spintronics due to their 100% spin polarization at the Fermi level (E_F), which is critical for spin

*These authors contributed equally to this work.
†Contact author: dibyaprakashrai@gmail.com
‡Contact author: kshrestha@wtamu.edu

injection. However, their performance is hindered by the presence of stray fields [21,22]. AFMs, in contrast, avoid stray fields and offer ultrafast spin dynamics at THz frequencies [23,24], but ultimately suppress the spin polarization at E_F. Furthermore, the coexistence of ferromagnetic and antiferromagnetic behavior in AM materials holds great promise for spintronics.

Examples of recently discovered collinear AFMs with nonrelativistic spin symmetry (NRSS) in the absence of SOC include RuO_2 [10,12,25], MnF_2 [19,26], FeF_2 [27], $FeSb_2$ [11], $MnP(S, Se)_3$ [28], Fe(S,Se) [28,29], MnTe [11], $LiFe_2F_6$ [30], RuF_4 [31], CrSb [32], Mn_5Si_3 [33], and others. Spin group theory, developed by Litvin *et al.* [34,35], has been utilized to establish selection rules for the AMs. The theoretical criteria proposed by Smejkal *et al.* [1] for identifying the AMs are as follows: (i) an even number of magnetic atoms in a unit cell, (ii) the presence of noninterconvertible local motif-pair anisotropy, (iii) the magnetic atoms in a unit cell not protected by inversion symmetry, and (iv) the opposite-spin sublattices connected by a $\pi/2$ rotation only.

$FeSb_2$ is known for its exceptionally high thermoelectric power at low temperatures [36]. The temperature dependence of resistivity reveals that $FeSb_2$ exhibits insulating behavior with two distinct upturns, suggesting the presence of two energy gaps [37]. However, angle-resolved photoemission spectroscopy (ARPES) results indicate the presence of metallic surface states, which characterize this material as a correlated topological Kondo insulator [38]. Recent electronic band structure calculations [11] reveal that $FeSb_2$ has several electronic bands crossing the Fermi level, confirming its metallic properties.

Here, we present the synthesis, magnetization, and high-field torque magnetometry studies of $FeSb_2$. Our magnetization data indicate an antiferromagnetic ground state below room temperature, and the torque signal measured up to 41 T demonstrates clear de Haas–van Alphen (dHvA) oscillations. Using density functional theory (DFT), we computed the electronic band structure and Fermi surface. Our results show that despite the antiferromagnetic coupling between Fe spins, the spin-polarized electronic bands exhibit ferromagneticlike characteristics, with a splitting between spin-up and spin-down states as large as 0.2 eV. These observations strongly suggest that $FeSb_2$ is an AM candidate compound.

II. METHODOLOGY

A. Computational methods

The electronic structure of $FeSb_2$ was computed using first-principles density functional theory (DFT). For this, we employed the open-access DFT-based computational package QUANTUM ESPRESSO (QE) [39–41]. Based on experimental guidance, antiferromagnetic coupling was set between the two Fe atoms, and an arbitrary on-site d-electron interaction potential of $U = 2.0$ eV was assigned to each Fe atom. The unit cell structure was optimized using the vc-relax algorithm combined with conjugate gradient (CG) diagonalization within the DFT+U approximation [42–45].

All electron exchange and correlation effects were treated within the generalized gradient approximation (GGA) [46], in addition to the Hubbard on-site Coulomb interaction ($+U$) formalism, known as GGA+U [43,44]. The kinetic energy cutoff for wave functions and the charge density cutoff were set to 70 and 750 Ry, respectively. The convergence criterion for self-consistency in total energy during the iterative process was set to 10^{-8} Ry. The first Brillouin zone was integrated using a fine k mesh of $24 \times 24 \times 24$ within Monkhorst's scheme [47]. Additionally, the spin-polarized band structure calculation was performed with a fully relativistic scalar potential incorporating SOC and GGA+U to verify potential band splitting.

B. Material synthesis and experimental setup

High-quality single crystals of $FeSb_2$ were grown via a conventional flux-based growth technique. A self-flux of Sb is used to provide a liquidous environment to begin a solid-state reaction at high temperatures. The flux mixture of Fe (pieces, 99.99%), and Sb (shot, 99.999%), purchased from Alfa Aesar, was loaded inside a Canfield crucible set with a flux ratio of 1:11 and then sealed inside a quartz tube filled with $\frac{1}{3}$-atm of Ar atmosphere. The tube was heated at a rate of 200 °C/hr to 1000 °C and kept there for 36 hours. Then the tube was cooled down continuously to 640 °C with a cooling rate of 2 °C/hr. The laboratory-grown shiny $FeSb_2$ single crystals of dimension $\sim 2 \times 2 \times 1$ mm^3 were separated from excess Sb flux through the centrifuge technique at 640 °C. $FeSb_2$ crystallizes in an orthorhombic structure with space group *Pnnm* (No. 58). The quality of the grown crystals was checked using powder x-ray diffraction of the ground crystals and then energy-dispersive x-ray spectral (EDS) studies of single crystals.

Magnetization measurements on the $FeSb_2$ single crystal were performed using a Quantum Design Magnetic Property Measurement System (MPMS-3), during a warming process in the temperature range of 1.8 to 300 K. Torque measurements were performed using a miniature piezoresistive cantilever to observe dHvA oscillations at the National High Magnetic Field Laboratory, Tallahassee, FL. A tiny single crystal of $FeSb_2$ was attached to the cantilever arm using vacuum grease and then mounted on a rotating platform of the measurement probe. The probe was slowly cooled down to the base temperature of 0.4 K. Two resistive elements on the cantilever were balanced at the base temperature before starting the field-dependence measurements. Magnetic fields were swept at each fixed temperature at a rate of 1.5 T/min.

III. RESULTS AND DISCUSSION

A. Scanning electron microscopy and magnetic susceptibility

The scanning electron microscope (SEM) image, along with the energy-dispersive x-ray spectroscopy (EDS)-measured regions of multiple single crystals, acquired using a tabletop scanning electron microscope (Hitachi TM4000Plus), is illustrated in Fig. 1(a). This figure highlights the specific areas where EDS measurements were conducted, corresponding to spectra labeled 12, 13, 14, 15, 16, and 17. Each spectrum represents a unique region from five different single crystals, where EDS analysis was used to determine the elemental composition. The atomic stoichiometry of iron

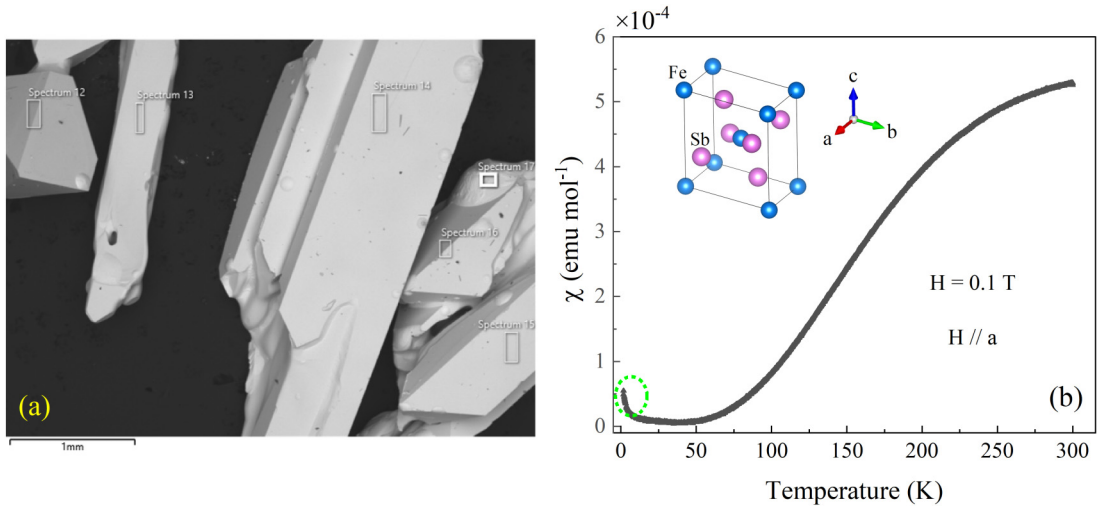

FIG. 1. (a) SEM image of the laboratory-grown single crystals of $FeSb_2$. The various regions highlighted by spectrum 12-17 represent the regions of analysis of the EDS spectrum. (b) Temperature dependence of the magnetic susceptibility, χ(T). Inset: The unit cell of $FeSb_2$, containing five Fe atoms: four at the corners and one at the center. χ(T) decreases with decreasing temperature, showing a slight upturn at low temperatures, highlighted by the dashed circle.

(Fe) and antimony (Sb) for each measured region is reported in Table I. Across most of the regions, specifically spectra 12 through 16, the EDS spectral analysis consistently shows an elemental stoichiometric ratio of Fe to Sb of approximately 1:2, which is within the resolution limit of the SEM. This ratio suggests that the crystal composition is homogeneous and well ordered. However, spectrum 17 has a deviation from this expected stoichiometry, which is attributed to contamination by residual flux on one of the crystal surfaces. This contamination likely affected the accuracy of the EDS measurement for that particular region, leading to an altered spectral response. Nonetheless, aside from this anomaly, the elemental analysis indicates uniformity in the stoichiometric ratios across the other regions, confirming the consistency of the material composition.

The zero-field-cooled (ZFC) magnetic susceptibility (χ) collected with an applied magnetic field of 0.1 T along the (1 0 0) crystallographic direction is presented in Fig. 1(b). The χ(T) value is notably small and exhibits a downward trend as the temperature decreases, indicating a suppression of magnetic susceptibility with cooling. This behavior signifies that the magnetic transition in $FeSb_2$ is antiferromagnetic type [48,49] and it happens at a temperature above room temperature (300 K). Earlier magnetic susceptibility investigations conducted by Rosenqvist [50] and Holseth and Kjekshus [51] reported that $FeSb_2$ exhibits antiferromagnetic behavior, with Néel temperatures (T_N) determined to be 773 K [50] and 1000 K [51], respectively. Consequently, our χ(T) measurements further validate the antiferromagnetic nature of $FeSb_2$. χ is 5×10^{-4} emu mol^{-1} at 300 K and decreases to $\sim 7 \times 10^{-6}$ emu mol^{-1} at 20 K. These values closely match those reported in previous studies, and χ(T) exhibits the same temperature dependence [52,53]. A weak upturn in χ(T) is observed at low temperature $\sim$10 K, as indicated by the dashed circle. This feature has been reported in previous studies [52,54] and may originate from a trace amount of an Fe-based secondary phase or change in the electronic interactions within the bulk sample.

TABLE I. Elemental analysis of energy-dispersive x-ray spectrum of various laboratory-grown $FeSb_2$ single crystals.

Spectrum = 12		Spectrum = 13	
Element	Atomic(%)	Element	Atomic(%)
Fe	33.49	Fe	32.43
Sb	66.5	Sb	67.56
Spectrum = 14		Spectrum = 15	
Element	Atomic (%)	Element	Atomic (%)
Fe	32.57	Fe	32.95
Sb	67.42	Sb	67.04
Spectrum = 16		Spectrum = 17	
Element	Atomic(%)	Element	Atomic (%)
Fe	32.97	Fe	0
Sb	67.02	Sb	100

B. High-field torque measurements

To map the Fermi surface of $FeSb_2$, we carried out torque measurements with the applied fields (H) up to 41 T. Figure 2(a) shows the temperature dependence of the torque (τ) for $FeSb_2$. The measurement was carried out at a tilt angle of $\theta = 28^\circ$, where θ is defined as the angle between the magnetic field and the c axis of the sample [Fig. 2(a), inset]. The τ signal varies nearly parabolically with H and shows clear and well-defined de Haas–van Alphen (dHvA) oscillations above 10 T. While increasing temperature, the amplitude of the dHvA oscillations decreases and the oscillation is still visible at 35 K. As seen in the graph, a single major frequency appears to be present, which can be confirmed by taking the Fourier transform of the data. Figure 2(b) is the frequency spectrum of the dHvA oscillations data shown in Fig. 2(a). As

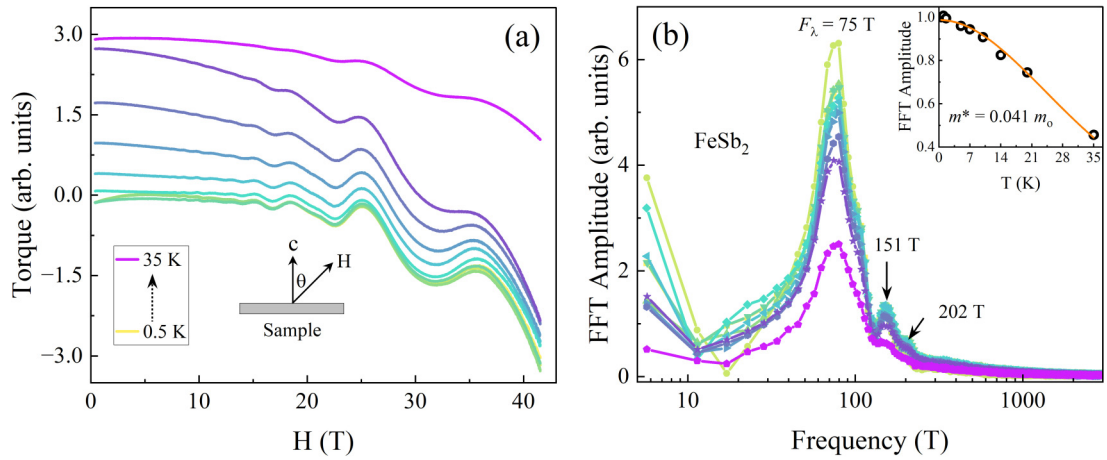

FIG. 2. (a) Torque τ measurements for a $FeSb_2$ single crystal at various temperatures up to 35 K, recorded at a tilt angle of $\theta = 28^\circ$. Distinct de Haas–van Alphen (dHvA) oscillations are observed above 10 T. (b) Frequency spectrum corresponding to the torque data in (a), displaying a prominent peak at 75 T, with additional peaks at 151 and 202 T. The x axis is plotted on a logarithmic scale to enhance the visibility of the frequency peaks. Inset: Lifshitz-Kosevich (LK) analysis of the temperature-dependent frequency data. The open circles represent the frequency amplitude, and the solid curve shows the best fit using the LK formula.

expected, there is a major frequency peak at $F_\lambda = 75$ T and two additional peaks at 151 and 202 T. It is important to note that 151 T is nearly twice the value of F_λ; therefore, this peak is likely to be the second harmonics of F_λ. The third peak at 202 T appears as a shallow shoulder and disappears quickly above 5 K. Therefore, we have not carried out a detailed analysis for this peak. The previous torque measurement of $FeSb_2$ [55] reported the presence of three frequencies between 60 and 120 T in the dHvA oscillation data.

As seen in Fig. 2(b), the amplitude of the frequency peak decreases at higher temperatures, consistent with the temperature-dependent behavior of dHvA oscillations in Fig. 2(a). The attenuation of the quantum oscillations signal with temperature and fields can be described by the Lifshitz-Kosevich (LK) theory [56]. In the inset in Fig. 2(b), the open circles show the amplitude of the fast Fourier transform (FFT) peak at different temperatures and the solid curve shows the best fit using the LK theory. From the best-fit parameter, we estimated the effective mass of charge carriers $m^* = 0.041 m_o$, where m_o is the rest mass of an electron. This value is slightly lower than that reported in a recent torque measurement of $FeSb_2$ [55].

To map the Fermi surface of $FeSb_2$, we rotated the sample within the magnetic field. According to Onsager's relation [48,57], the frequency of quantum oscillations is directly proportional to the cross-sectional area of the Fermi surface. Thus, by tracking the dHvA frequency at various θ values, we can effectively map the Fermi surface of this material [56,58–62]. Figure 3(a) shows the torque signal of $FeSb_2$ at selected θ values. The dHvA oscillation is not clearly visible at some angles; therefore, we subtracted a smooth polynomial background from the torque signal. Figure 3(b) shows the background-subtracted torque data and, as expected, the dHvA oscillations are visible at all angles. The oscillation period appears to change with different tilt angles, indicating that the frequency varies with angle. We plotted the angular variation of the frequency spectrum for $FeSb_2$, as depicted in Fig. 3(c). The frequency exhibits a weak angular dependence, suggesting a nearly isotropic Fermi surface cross section. As seen in the graph, there is a major peak F_λ, which appears to split while changing $\theta = 42^\circ$ to 56° and 70°. We tracked the variation of F_λ at different angles and show its angular variation in Fig. 3(d). F_λ initially increases and decreases at higher angles. The possible theoretical frequencies computed from the DFT are also included in the plot for comparison. The frequency values are comparable and will be further discussed later.

C. Electronic bands and Fermi surface

In order to understand the electronic structure of $FeSb_2$, we have calculated the electronic bands and Fermi surface using the DFT. $FeSb_2$ also possesses a motif-pair anisotropy with collinear antiferromagnetic coupling between two Fe atoms, as in RuO_2 [1,63]. The local environment around Fe1 and Fe2 atoms is governed by the $\pi/2$ rotational symmetry and the $\mathcal{T}$ flips the spin of the two magnetic atoms [Fig. 4(a)]. For a comprehensive study of the electronic profile, we have calculated the band structure of $FeSb_2$ by considering both spin-polarized and SOC setups [Figs. 4(c) and 4(d)]. For sampling, the band path we have considered is $S - Y' - \Gamma - Y - A - Z - A'$ as the optimum path of high-symmetry points within the first Brillouin zone, as shown in Fig. 4(b). The spin-polarized band structure shows antisymmetric bands occurring between the spin-up and spin-down states, despite the antiferromagnetic coupling between the two Fe atoms. The nature of the spin-polarized band structure displays typical behavior of a ferromagnetic band. This characteristic suggests the possible presence of spin band splitting, attributed to the broken $\mathcal{T}$ symmetry. The NRSS around the high-symmetry point of a collinear AFM with compensated magnetization, without implementing SOC, is a clear signature of an AM [1–4,12,14].

The nondegenerate band at the Γ point splits up into spin-up and spin-down along the $Y' - \Gamma$ and $\Gamma - Y$ symmetry paths at the Fermi level. A similar feature of band splitting has

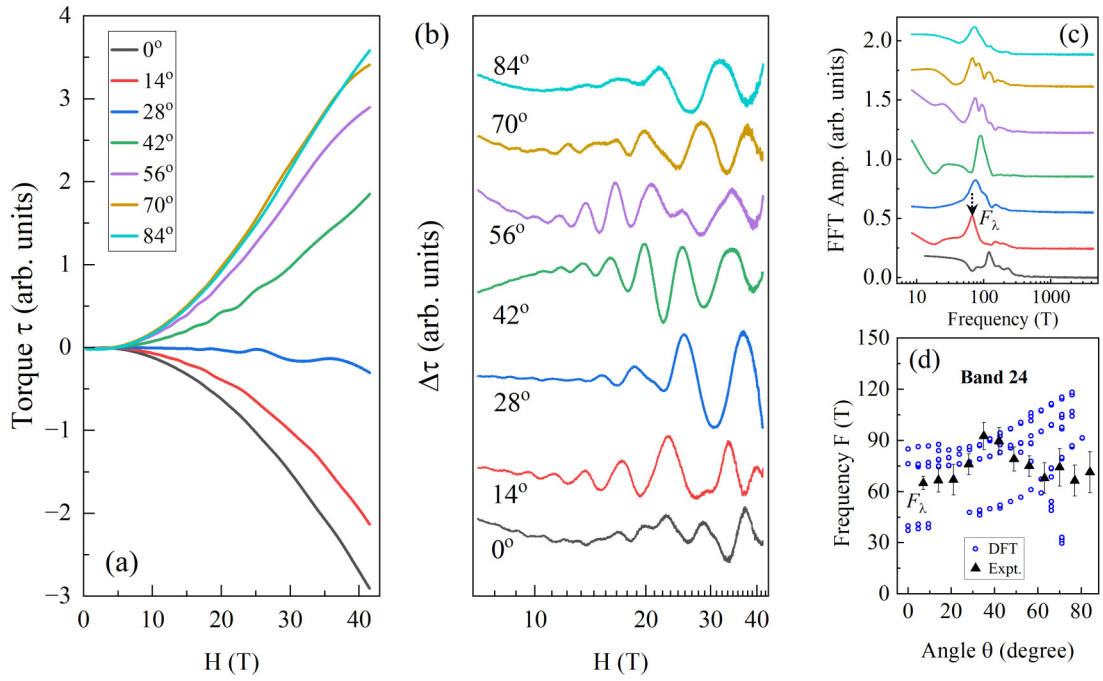

FIG. 3. (a) Torque (τ) data for a FeSb2 single crystal at selected tilt angles (θ). The sample's torque response changes with the applied magnetic field as it is rotated, showing de Haas–van Alphen (dHvA) oscillations. (b) Background-subtracted torque data for different θ values, where quantum oscillations are visible and seem to shift in period as θ changes. (c) Frequency spectrum of the data shown in (b). The dashed arrow indicates the position of the major peak (F_λ) in the spectrum. The x axis is plotted on a logarithmic scale for better visibility. (d) Angular variation of F_λ with θ. The frequency initially increases, but decreases at higher angles above 40°. Theoretical frequencies derived from band 24 are shown in open circles.

also been observed in $A - Z$ and $Z - A'$ symmetry around the Fermi energy [Fig. 5(a)]. The distinctive spin splitting and the Fermi crossing are contributed by the bands 24 and 26 (spin up and spin down). We have also observed the presence of a flat band above the Fermi energy along the $Y' - \Gamma$ and $\Gamma - Y$ symmetries exhibited by band 25 (spin-up and spin-down). The strength of spin splitting (Δ) around the Fermi energy is determined by subtracting the energy for the up and down spins, that is, $E(\uparrow) - E(\downarrow) = |\Delta|$, and is plotted in Figs. 5(b) and 5(c). $|\Delta|$ varies along the symmetry path and reaches the

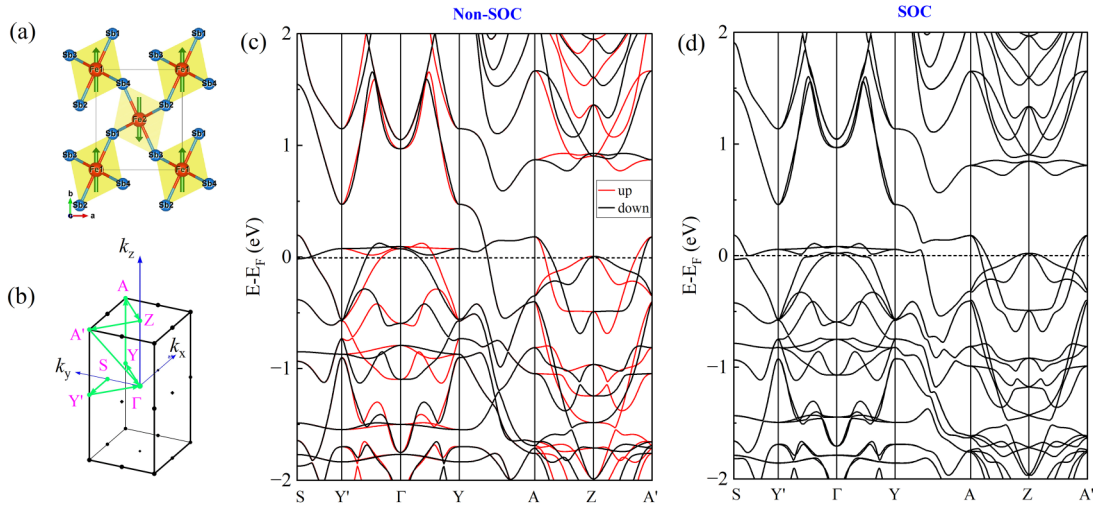

FIG. 4. (a) Top view of $FeSb_2$ structure in the xy plane, where two magnetic atoms are associated with the magnetic vectors representing spin up and spin down (green arrows). The two Fe atoms in the unit cell are linked with four Sb atoms, creating a local environment of yellow-shaded polyhedra called the motif. (b) First Brillouin zone showing high-symmetry points. Note that Y′ and A′ are positioned at coordinates opposite to Y and A, respectively. Electronic band structure of $FeSb_2$: spin-polarized calculation (c) without spin-orbit coupling (SOC) and (d) with SOC. Three bands, i.e., 24, 25, and 26, intersect the Fermi level, showing $FeSb_2$'s metallic properties.

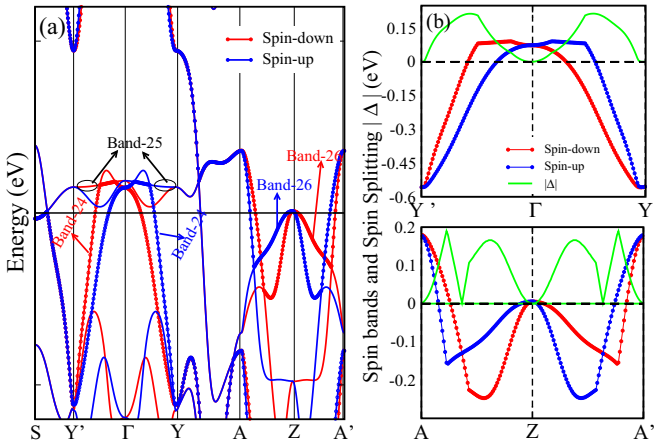

FIG. 5. (a) Band crossing of flat band and spin bands. (b) Band splitting ($|\Delta|$), near the Fermi level. The $|\Delta|$ reaches a maximum value of ~ 0.2 eV along $A - Z - A'$ (bottom panel).

maximum value of ~ 0.2 eV. The $|\Delta|$ value is quite smaller than that of the prototype AM RuO_2 [2,64], which has a value of 1.4 eV, but it is consistent with a recent DFT report on $FeSb_2$ [11].

The relativistic band structure, calculated by considering the SOC effect, is presented in Fig. 4(b). Our SOC band clearly captures the features of the non-SOC spin-polarized bands (spin up and spin down). Three bands-24, 25, and 26-cross the Fermi level and contribute to the Fermi surface of $FeSb_2$. We have calculated the Fermi surface for both the spin-up and spin-down bands that cross the Fermi level. The Fermi surfaces, represented by two antisymmetric blue and green lobes (with d-wave symmetry) near the Γ point, are due to the spin-up and spin-down bands and correspond to band 24 [Fig. 6(a)]. The Fermi surfaces shown in Figs. 6(b) and 6(c) correspond to band 26, which crosses the Fermi level at different locations within the first Brillouin zone along the $A' - Z - A$ symmetry (Fig. 5).

According to Onsager's relation [56,65], the frequency of quantum oscillation is directly proportional to the cross section of the Fermi surface. In order to compare experimentally observed dHvA frequencies, we computed theoretical frequencies using the Onsager relationship [66]. For this, we used the SKEAF code [67] to extract the theoretical frequencies from the Fermi surface cross-sectional area. Figure 3(d) shows the angular dependence of the dHvA frequency F_λ, along with the theoretical frequencies computed from band 24. In the graph, $F_\lambda = 65$ T, which is comparable to the DFT-calculated value of approximately 75 T at $\theta = 0°$. There appears a small variation frequency with θ, where F_λ initially increases and then begins to decrease. Since frequency measures the Fermi surface cross section [56,68], the weak angular dependence of frequency suggests a nearly isotropic Fermi surface cross section. This is also reflected in the nearly spherical Fermi surface pocket observed for band 24.

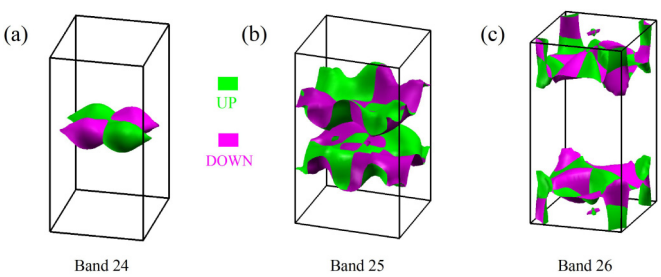

FIG. 6. Fermi surfaces of $FeSb_2$ depicting spin-up (green) and spin-down (magenta) bands crossing the Fermi level. Three bands, i.e., 24, 25, and 26, contribute to the Fermi surface.

IV. SUMMARY

To summarize, we have presented the synthesis and detailed electronic structure studies of $FeSb_2$ through high-field torque magnetometry and density functional theory (DFT) calculations. The temperature dependence of magnetic susceptibility shows the antiferromagnetic behavior below 300 K. It is important to note the weak upturn observed below 10 K in the susceptibility data [Fig. 1(b)], a feature that has also been reported in previous studies [52,54]. Although spectroscopic data and single-crystal analysis indicate a predominantly single-phase sample, we propose that this minor upturn may result from either a trace amount of Fe-based secondary phase contributing a small magnetic signal or from changes in the electronic interactions within the material. Further investigation into the specific nature or phase of this Fe-related compound would provide valuable insights for future work. To understand the electronic properties of $FeSb_2$, we performed high-field torque magnetometry with the applied field up to 41 T and the torque signal showed visible de Haas–van Alphen (dHvA) oscillations. By analyzing the temperature and angular dependence measurements of dHvA quantum oscillations, we estimated the effective mass of the charge carriers and mapped the Fermi surface cross section of $FeSb_2$. We observed a prominent frequency peak near 65 T, which shows only slight variation when the sample is rotated in a magnetic field. This indicates that the frequency originates from a nearly isotropic Fermi surface.

It is important to note that Tang *et al.* [55] reported a high-frequency torque measurement in $FeSb_2$ and identified three frequencies in dHvA oscillations between 60 and 120 T. Using scanning electron microscopy (SEM), the authors observed embedded antimony flux within or on the surface of the crystals. The quantum oscillations disappeared once the embedded antimony was removed by polishing, and the authors suggested that the dHvA oscillations might have originated from the embedded antimony crystal. However, quantum oscillations in materials are highly dependent on the crystallinity of the sample, with high-quality, well-crystallized samples being essential for their observation. Polishing a single crystal can create a rougher surface, causing it to behave more like a polycrystalline material, which may suppress quantum oscillations. This effect could explain the absence of oscillations in the polished $FeSb_2$ samples studied by Tang *et al.* [55]. In our experiments, we carefully analyzed the crystals using SEM [Fig. 1(a)] and found no trace of antimony flux on the $FeSb_2$ crystals. Additionally, torque measurements were conducted only on SEM-verified crystals. Therefore, it is unlikely

that the dHvA signals observed in our torque measurements (Figs. 2 and 3) originate from any embedded antimony.

For a deeper understanding of its electronic profile, we used DFT to calculate the electronic bands and Fermi surface. Remarkably, the calculated bands exhibit a distinct spin splitting in the compensated collinear antiferromagnetic state, with the splitting amplitude reaching up to 0.2 eV. This spin splitting, despite the antiferromagnetic coupling between Fe spins, aligns with features characteristic of altermagnetic behavior. Three electronic bands cross the Fermi level, contributing to the Fermi surface of $FeSb_2$. The Fermi surface exhibits anisotropic features in the spin-up and spin-down pockets, displaying d-wave symmetry. We calculated theoretical frequencies based on the Fermi pocket cross-sectional areas and compared them with the experimentally observed dHvA frequencies. Although $FeSb_2$ has been known for a long time, its electronic and magnetic properties have not been well explored. The comprehensive analysis presented in this work strongly suggests that $FeSb_2$ exhibits altermagnetic characteristics, providing a promising pathway for the discovery of new altermagnetic systems.

ACKNOWLEDGMENTS

The work at the West Texas A&M University (WTAMU) is supported by the Killgore Undergraduate and Graduate Student Research Grants, the Welch Foundation (Grant No. AE-0025), and the National Science Foundation (Award ID No. 2336011). The computations were performed on the WTAMU HPC cluster, which was funded by the National Science Foundation (NSF CC* GROWTH Grant No. 2018841). G.P. gratefully acknowledges the support of the University of West Georgia and University of California, Santa Barbara. G.P. would also like to thank Prof. Stephen D. Wilson for his support and insightful discussions. A portion of this work was performed at the National High Magnetic Field Laboratory, which is supported by National Science Foundation Cooperative Agreement No. DMR-2128556 and the State of Florida.

[1] L. Šmejkal, J. Sinova, and T. Jungwirth, Emerging research landscape of altermagnetism, Phys. Rev. X **12**, 040501 (2022).

[2] L. Šmejkal, R. Gonzalez-Hernandez, T. Jungwirth, and J. Sinova, Crystal time-reversal symmetry breaking and spontaneous Hall effect in collinear antiferromagnets, Sci. Adv. **6**, eaaz8809 (2020).

[3] S. Hayami, Y. Yanagi, and H. Kusunose, Momentum-dependent spin splitting by collinear antiferromagnetic ordering, J. Phys. Soc. Jpn. **88**, 123702 (2019).

[4] L. D. Yuan and A. Zunger, Degeneracy removal of spin bands in collinear antiferromagnets with non-interconvertible spin-structure motif pair, Adv. Mater. **35**, 2211966 (2023).

[5] X. Zhou, H. Liu, W. Wu, K. Jiang, Y. Shi, Z. Li, Y. Sui, J. Hu, and J. Luo, Anomalous thermal Hall effect and anomalous Nernst effect of CsV_3Sb_5, Phys. Rev. B **105**, 205104 (2022).

[6] Z. Feng, X. Zhou, L. Šmejkal, L. Wu, Z. Zhu, H. Guo, R. Gonzalez-Hernandez, X. Wang, H. Yan, P. Qin, X. Zhang, H. Wu, H. Chen, Z. Meng, L. Liu, Z. Xia, J. Sinova, T. Jungwirth, and Z. Liu, An anomalous Hall effect in altermagnetic ruthenium dioxide, Nat. Electron. **5**, 735 (2022).

[7] Z. H. Zhu, J. Strempfer, R. R. Rao, C. A. Occhialini, J. Pelliciari, Y. Choi, T. Kawaguchi, H. You, J. F. Mitchell, Y. Shao-Horn, and R. Comin, Anomalous antiferromagnetism in metallic RuO_2 determined by resonant x-ray scattering, Phys. Rev. Lett. **122**, 017202 (2019).

[8] R. M. Sattigeri, G. Cuono, and C. Autieri, Altermagnetic surface states: towards the observation and utilization of altermagnetism in thin films, interfaces and topological materials, Nanoscale **15**, 16998 (2023).

[9] I. I. Mazin, Altermagnetism in MnTe: Origin, predicted manifestations, and routes to detwinning, Phys. Rev. B **107**, L100418 (2023).

[10] L. Šmejkal, A. Marmodoro, K.-H. Ahn, R. Gonzalez-Hernandez, I. Turek, S. Mankovsky, H. Ebert, S. W. D'Souza, O. Šipr, J. Sinova, and T. Jungwirth, Chiral magnons in altermagnetic RuO_2, Phys. Rev. Lett. **131**, 256703 (2023).

[11] I. I. Mazin, K. Koepernik, M. D. Johannes, R. Gonzalez-Hernandez, and L. Šmejkal, Prediction of unconventional magnetism in doped $FeSb_2$, Proc. Natl. Acad. Sci. USA **118**, e2108924118 (2021).

[12] L. Šmejkal, J. Sinova, and T. Jungwirth, Beyond conventional ferromagnetism and antiferromagnetism: A phase with nonrelativistic spin and crystal rotation symmetry, Phys. Rev. X **12**, 031042 (2022).

[13] P. A. McClarty and J. G. Rau, Landau theory of altermagnetism (unpublished).

[14] I. Mazin, Editorial: Altermagnetism - A new punch line of fundamental magnetism, Phys. Rev. X **12**, 040002 (2022).

[15] O. Gomonay, V. Baltz, A. Brataas, and Y. Tserkovnyak, Antiferromagnetic spin textures and dynamics, Nat. Phys. **14**, 213 (2018).

[16] D. F. Shao, S. H. Zhang, M. Li, C. B. Eom, and E. Y. Tsymbal, Spin-neutral currents for spintronics, Nat. Commun. **12**, 7061 (2021).

[17] L. Šmejkal, A. B. Hellenes, R. Gonzalez-Hernandez, J. Sinova, and T. Jungwirth, Giant and tunneling magnetoresistance in unconventional collinear antiferromagnets with nonrelativistic spin-momentum coupling, Phys. Rev. X **12**, 011028 (2022).

[18] R. D. G. Betancourt, J. Zubac, R. Gonzalez-Hernandez, K. Geishendorf, Z. Soban, G. Springholz, K. Olejník, L. Šmejkal, J. Sinova, T. Jungwirth, S. T. B. Goennenwein, A. Thomas, H. Reichlová, J. Železný, and D. Kriegner, Spontaneous anomalous Hall effect arising from an unconventional compensated magnetic phase in a semiconductor, Phys. Rev. Lett. **130**, 036702 (2023).

[19] S. Bhowal and N. A. Spaldin, Ferroically ordered magnetic octupoles in d-wave altermagnets, Phys. Rev. X **14**, 011019 (2024).

[20] A. Soumyanarayanan, N. Reyren, A. Fert, and C. Panagopoulos, Emergent phenomena induced by spin-orbit coupling at surfaces and interfaces (unpublished).

[21] X. Marti, I. Fina, C. Frontera, J. Liu, P. Wadley, Q. He, R. Paull, J. Clarkson, J. Kudrnovský, I. Turek, J. Kuneš, D. Yi, J.-H. Chu, C. Nelson, L. You, E. Arenholz, S. Salahuddin, J. Fontcuberta, T. Jungwirth, and R. Ramesh, Room-temperature antiferromagnetic memory resistor, Nat. Mater. **13**, 367 (2014).

[22] S. Jenkins, A. Meo, L. E. Elliott, S. K. Piotrowski, M. Bapna, R. W. Chantrell, S. A. Majetich, and R. F. L. Evans, Magnetic stray fields in nanoscale magnetic tunnel junctions, J. Phys. D **53**, 044001 (2020).

[23] D. Yang, W. Wen, C. Xu, K. Lee, T. Yu, and H. Yang, Electrically tunable terahertz resonance in antiferromagnetic NiO/Pt Heterostructures, Phys. Rev. Appl. **20**, 014023 (2023).

[24] S. Hu, C. Zheng, W. Fan, and Y. Liu, Terahertz magnetic excitations in noncollinear antiferromagnetic Mn_3Pt: Atomistic-scale dynamical simulations, J. Magn. Magn. Mater. **588**, 171393 (2023).

[25] Y. Huang, J. Lai, J. Zhan, T. Yu, R. Chen, P. Liu, X.-Q. Chen, and Y. Sun, *Ab initio* study of quantum oscillations in altermagnetic and nonmagnetic phases of RuO_2, Phys. Rev. B **110**, 144410 (2024).

[26] N. N. Orlova, A. A. Avakyants, A. V. Timonina, N. N. Kolesnikov, and E. V. Deviatov, Crossover from relativistic to nonrelativistic net magnetization for MnTe altermagnet candidate, JETP Lett. **120**, 360 (2024).

[27] D. C. Joshi, P. Nordblad, and R. Mathieu, Ferromagnetic excess moments and apparent exchange bias in FeF_2 single crystals, Sci. Rep. **9**, 18884 (2019).

[28] I. Mazin, R. González-Hernández, and L. Šmejkal, Induced monolayer altermagnetism in $MnP(S,Se)_3$ and FeSe, arXiv:2309.02355.

[29] Q. Liu, J. Kang, P. Wang, W. Gao, Y. Qi, J. Zhao, and X. Jiang, Inverse magnetocaloric effect in altermagnetic 2D non-van der Waals FeX (X = S and Se) semiconductors, Adv. Funct. Mater. **34**, 2402080 (2024).

[30] P.-J. Guo, Y. Gu, Z.-F. Gao, and Z.-Y. Lu, Altermagnetic ferroelectric $life_2f_6$ and spin-triplet excitonic insulator phase, arXiv:2312.13911.

[31] M. Milivojević, M. Orozović, S. Picozzi, M. Gmitra, and S. Stavrić, Interplay of altermagnetism and weak ferromagnetism in two-dimensional RuF_4, 2D Mater. **11**, 035025 (2024).

[32] Y. Guo, H. Liu, O. Janson, I. C. Fulga, J. van den Brink, and J. I. Facio, Spin-split collinear antiferromagnets: A large-scale *ab initio* study, Mater. Today Phys. **32**, 100991 (2023).

[33] H. Reichlova, R. L. Seeger, R. González-Hernández *et al.*, Observation of a spontaneous anomalous Hall response in the Mn_5Si_3d-wave altermagnet candidate, Nat. Commun. **15**, 4961 (2023).

[34] D. B. Litvin, Spin point groups, Acta Crystallogr. Sec. A: Crystal Phys. Diffract. Theoret. General Crystallogr. **33**, 279 (1977).

[35] D. B. Litvin, Wreath groups—Symmetry of crystals with structural distortions, Phys. Rev. B **21**, 3184 (1980).

[36] C. C. Homes, Q. Du, C. Petrovic, W. Brito, S. Choi, and G. Kotliar, Unusual electronic and vibrational properties in the colossal thermopower material $FeSb_2$, Sci. Rep. **8**, 11692 (2018).

[37] H. Takahashi, R. Okazaki, I. Terasaki, and Y. Yasui, Origin of the energy gap in the narrow-gap semiconductor $FeSb_2$ revealed by high-pressure magnetotransport measurements, Phys. Rev. B **88**, 165205 (2013).

[38] K.-J. Xu, S.-D. Chen, Y. He, J. He, S. Tang, C. Jia, E. Yue Ma, S.-K. Mo, D. Lu, M. Hashimoto *et al.*, Metallic surface states in a correlated d-electron topological Kondo insulator candidate $FeSb_2$, Proc. Natl. Acad. Sci. USA **117**, 15409 (2020).

[39] P. Giannozzi, S. Baroni, N. Bonini, M. Calandra, R. Car, C. Cavazzoni, D. Ceresoli, G. L. Chiarotti, M. Cococcioni, I. Dabo, A. Dal Corso, S. De Gironcoli, S. Fabris, G. Fratesi, R. Gebauer, U. Gerstmann, C. Gougoussis, A. Kokalj, M. Lazzeri, L. Martin-Samos *et al.*, QUANTUM ESPRESSO: A modular and open-source software project for quantum simulations of materials, J. Phys.: Condens. Matter **21**, 395502 (2009).

[40] P. Giannozzi, O. Andreussi, T. Brumme, O. Bunau, M. B. Nardelli, M. Calandra, R. Car, C. Cavazzoni, D. Ceresoli, M. Cococcioni, N. Colonna, I. Carnimeo, A. Dal Corso, S. De Gironcoli, P. Delugas, R. A. Distasio, A. Ferretti, A. Floris, G. Fratesi, G. Fugallo *et al.*, Advanced capabilities for materials modelling with QUANTUM ESPRESSO, J. Phys.: Condens. Matter **29**, 465901 (2017).

[41] P. Giannozzi, O. Baseggio, P. Bonfà, D. Brunato, R. Car, I. Carnimeo, C. Cavazzoni, S. De Gironcoli, P. Delugas, F. F. Ruffino, A. Ferretti, N. Marzari, I. Timrov, A. Urru, and S. Baroni, QUANTUM ESPRESSO toward the exascale, J. Chem. Phys. **152**, 154105 (2020).

[42] M. Cococcioni and S. de Gironcoli, Linear response approach to the calculation of the effective interaction parameters in the LDA+U method, Phys. Rev. B **71**, 035105 (2005).

[43] V. I. Anisimov, I. V. Solovyev, M. A. Korotin, M. T. Czyzyk, and G. A. Sawatzky, Density-functional theory and NiO photoemission spectra, Phys. Rev. B **48**, 16929 (1993).

[44] S. L. Dudarev, L.-M. Peng, S. Y. Savrasov, and J.-M. Zuo, Correlation effects in the ground-state charge density of Mott insulating NiO: A comparison of *ab initio* calculations and high-energy electron diffraction measurements, Phys. Rev. B **61**, 2506 (2000).

[45] K. Nawa and Y. Miura, Exploring half-metallic Co-based full Heusler alloys using a DFT+U method combined with linear response approach, RSC Adv. **9**, 30462 (2019).

[46] J. P. Perdew, K. Burke, and M. Ernzerhof, Generalized gradient approximation made simple, Phys. Rev. Lett. **77**, 3865 (1996).

[47] H. J. Monkhorst and J. D. Pack, Special points for Brillouin-zone integrations, Phys. Rev. B **13**, 5188 (1976).

[48] C. Kittel, *Introduction to Solid State Physics* (Wiley, New York, 2018).

[49] N. W. Ashcroft and N. Mermin, *Solid State Physics* (Holt, Rinehart and Winston, New York, 1976).

[50] T. Rosenqvist, Magnetic and crystallographic studies on the higher antimonies of iron, cobalt and nickel, Acta Metall. **1**, 761 (1953).

[51] H. Holseth and A. Kjekshus, Compounds with the marcasite type crystal structure III. On the magnetic properties of the binary pnictides, J. Less-Common Met. **16**, 472 (1968).

[52] C. G. da Silva, Magnetic susceptibility of $FeSb_2$: A quasimagnetic semiconductor, Solid State Commun. **33**, 63 (1980).

[53] A. K. Fan, G. H. Rosenthal, H. L. McKinzie, and A. Wold, Preparation and properties of $FeAs_2$ and $FeSb_2$, J. Solid State Chem. **5**, 136 (1972).

[54] H. Takahashi, Y. Yasui, I. Terasaki, and M. Sato, Effects of ppm-level imperfection on the transport properties of $FeSb_2$ single crystals, J. Phys. Soc. Jpn. **80**, 054708 (2011).

[55] F. Tang, Q. Du, C. Petrovic, W. Zhang, M. He, and L. Zhang, Negative differential resistance and quantum oscillations in $FeSb_2$ with embedded antimony, Chin. Phys. B **28**, 037104 (2019).

[56] D. Shoenberg, *Magnetic Oscillations in Metals* (Cambridge University Press, Cambridge, 1984).

[57] T. Nguyen, N. Aryal, B. K. Pokharel, L. Harnagea, D. Mierstchin, D. Popović, D. E. Graf, and K. Shrestha, Fermiology of the Dirac type-II semimetal candidates (Ni, Zr)Te_2 using de Haas–van Alphen oscillations, Phys. Rev. B **106**, 075154 (2022).

[58] C. Phillips, K. Shtefiienko, T. Nguyen, A. N. C. Salinas, B. A. Magar, G. Pokharel, S. D. Wilson, D. E. Graf, and K. Shrestha, Fermi surface reconstruction under pressure in the kagome metal CsV_3Sb_5, Phys. Rev. B **110**, 205135 (2024).

[59] B. R. Ortiz, P. M. Sarte, E. M. Kenney, M. J. Graf, S. M. L. Teicher, R. Seshadri, and S. D. Wilson, Superconductivity in the kagome metal, Phys. Rev. Mater. **5**, 034801 (2021).

[60] A. A. Taskin and Y. Ando, Berry phase of nonideal Dirac fermions in topological insulators, Phys. Rev. B **84**, 035301 (2011).

[61] K. Shrestha, V. Marinova, B. Lorenz, and P. C. W. Chu, Shubnikov–de Haas oscillations from topological surface states of metallic $Bi_2Se_{2.1}Te_{0.9}$, Phys. Rev. B **90**, 241111(R) (2014).

[62] K. Shrestha, M. Shi, T. Nguyen, D. Miertschin, K. Fan, L. Deng, D. E. Graf, X. Chen, and C.-W. Chu, Fermi surface mapping of the kagome superconductor RbV_3Sb_5 using de Haas-van Alphen oscillations, Phys. Rev. B **107**, 075120 (2023).

[63] C.-C. Wei, E. Lawrence, A. Tran, and H. Ji, Crystal chemistry and design principles of altermagnets, ACS Organ. Inorgan. Au **4**, 604 (2024).

[64] K.-H. Ahn, A. Hariki, K.-W. Lee, and J. Kuneš, Antiferromagnetism in RuO_2 as d-wave Pomeranchuk instability, Phys. Rev. B **99**, 184432 (2019).

[65] K. Shrestha, B. Regmi, G. Pokharel, S.-G. Kim, S. D. Wilson, D. E. Graf, B. A. Magar, C. Phillips, and T. Nguyen, Electronic properties of kagome metal ScV_6Sn_6 using high-field torque magnetometry, Phys. Rev. B **108**, 245119 (2023).

[66] K. Shrestha, M. Shi, B. Regmi, T. Nguyen, D. Miertschin, K. Fan, L. Z. Deng, N. Aryal, S.-G. Kim, D. E. Graf, X. Chen, and C. W. Chu, High quantum oscillation frequencies and nontrivial topology in kagome superconductor KV_3Sb_5 probed by torque magnetometry up to 45 T, Phys. Rev. B **107**, 155128 (2023).

[67] S. Julian, Numerical extraction of de Haas–van Alphen frequencies from calculated band energies, Comput. Phys. Commun. **183**, 324 (2012).

[68] K. Shrestha, R. Chapai, B. K. Pokharel, D. Miertschin, T. Nguyen, X. Zhou, D. Y. Chung, M. G. Kanatzidis, J. F. Mitchell, U. Welp, D. Popovic, D. E. Graf, B. Lorenz, and W. K. Kwok, Nontrivial Fermi surface topology of the kagome superconductor CsV_3Sb_5 probed by de Haas–van Alphen oscillations, Phys. Rev. B **105**, 024508 (2022).